Extended-image-based correction of aberrations using a deformable mirror with hysteresis

ORESTIS KAZASIDIS,[1,*] SVEN VERPOORT,[1] OLEG SOLOVIEV,[2] GLEB VDOVIN,[2] MICHEL VERHAEGEN,[2] AND ULRICH WITTROCK[1]

[1]*Photonics Laboratory, Münster University of Applied Sciences, Stegerwaldstrasse 39, 48565 Steinfurt, Germany*
[2]*Delft Center for System and Control, Delft University of Technology, Mekelweg 2, 2628 CD Delft, The Netherlands*
[*]kazasidis@fh-muenster.de

Abstract: With a view to the next generation of large space telescopes, we investigate guide-star-free, image-based aberration correction using a unimorph deformable mirror in a plane conjugate to the primary mirror. We designed and built a high-resolution imaging testbed to evaluate control algorithms. In this paper we use an algorithm based on the heuristic hill climbing technique and compare the correction in three different domains, namely the voltage domain, the domain of the Zernike modes, and the domain of the singular modes of the deformable mirror. Through our systematic experimental study, we found that successive control in two domains effectively counteracts uncompensated hysteresis of the deformable mirror.

References and links

1. M. D. Lallo, "Experience with the Hubble Space Telescope: 20 years of an archetype," Optical Engineering **51**, 011011 (2012).
2. J. T. Trauger, D. C. Moody, J. E. Krist, and B. L. Gordon, "Hybrid Lyot coronagraph for WFIRST-AFTA: coronagraph design and performance metrics," Journal of Astronomical Telescopes, Instruments, and Systems **2**, 011013 (2016).
3. F. Shi, K. Balasubramanian, R. Hein, R. Lam, D. Moore, J. Moore, K. Patterson, I. Poberezhskiy, J. Shields, E. Sidick, H. Tang, T. Truong, J. K. Wallace, X. Wang, and D. Wilson, "Low-order wavefront sensing and control for WFIRST-AFTA coronagraph," Journal of Astronomical Telescopes, Instruments, and Systems **2**, 011021 (2016).
4. AURA Report, "From Cosmic Birth to Living Earths," http://www.hdstvision.org/report (2015).
5. B. H. Dean and C. W. Bowers, "Diversity selection for phase-diverse phase retrieval," J. Opt. Soc. Am. A **20**, 1490–1504 (2003).
6. A. Give'on, B. D. Kern, and S. Shaklan, "Pair-wise, deformable mirror, image plane-based diversity electric field estimation for high contrast coronagraphy," Proc. SPIE **8151**, 815110 (2011).
7. M. W. Warmuth, S. W. Parker, A. J. Wilson, K. W. Gleichman, R. G. Paxman, B. J. Thelen, R. J. Murphy, J. D. Hunt, and J. W. LeBlanc, "Operation of phase-diverse adaptive-optics with extended scenes," Proc. SPIE **7093**, 709307 (2008).
8. M. J. Booth, "Wave front sensor-less adaptive optics: a model-based approach using sphere packings," Opt. Express **14**, 1339–1352 (2006).
9. M. J. Booth, "Wavefront sensorless adaptive optics for large aberrations," Opt. Lett. **32**, 5–7 (2007).
10. H. Linhai and C. Rao, "Wavefront sensorless adaptive optics: a general model-based approach," Opt. Express **19**, 371–379 (2011).
11. H. Yang, O. Soloviev, and M. Verhaegen, "Model-based wavefront sensorless adaptive optics system for large aberrations and extended objects," Opt. Express **23**, 24587–24601 (2015).
12. J. Mertz, H. Paudel, and T. G. Bifano, "Field of view advantage of conjugate adaptive optics in microscopy applications," Appl. Opt. **54**, 3498–3506 (2015).
13. S. Bonora and R. J. Zawadzki, "Wavefront sensorless modal deformable mirror correction in adaptive optics: optical coherence tomography," Opt. Lett. **38**, 4801–4804 (2013).
14. Y. N. Sulai and A. Dubra, "Non-common path aberration correction in an adaptive optics scanning ophthalmoscope," Biomed. Opt. Express **5**, 3059–3073 (2014).
15. D. J. Wahl, Y. Jian, S. Bonora, R. J. Zawadzki, and M. V. Sarunic, "Wavefront sensorless adaptive optics fluorescence biomicroscope for in vivo retinal imaging in mice," Biomed. Opt. Express **7**, 1–12 (2016).
16. P. Rausch, S. Verpoort, and U. Wittrock, "Unimorph deformable mirror for space telescopes: environmental testing," Opt. Express **24**, 1528–1542 (2016).

17. L. P. Murray, J. C. Dainty, J. Coignus, and F. Felberer, "Wavefront correction of extended objects through image sharpness maximisation," Proc. SPIE **6018**, 60181A (2005).
18. B. Dong and J. Yu, "Hybrid approach used for extended image-based wavefront sensor-less adaptive optics," Chin. Opt. Lett. **13**, 041101–041101 (2015).
19. T. E. Agbana, H. Yang, O. Soloviev, G. Vdovin, and M. Verhaegen, "Sensorless adaptive optics system based on image second moment measurements," Proc. SPIE **9896**, 989609 (2016).
20. P. Rausch, S. Verpoort, and U. Wittrock, "Unimorph deformable mirror for space telescopes: design and manufacturing," Opt. Express **23**, 19469–19477 (2015).
21. G. D. Boreman, *Modulation Transfer Function in Optical and Electro-Optical Systems* (SPIE, 2001).
22. S. Verpoort and U. Wittrock, "Actuator patterns for unimorph and bimorph deformable mirrors," Appl. Opt. **49**, G37–G46 (2010).
23. J. C. Wyant and K. Creath, "Basic wavefront aberration theory for optical metrology," in *Applied Optics and Optical Engineering*, R. R. Shannon and J. C. Wyant, eds. (Academic, Inc., 1992, Vol. 11).
24. J. Perchermeier and U. Wittrock, "Precise measurements of the thermo-optical aberrations of an Yb:YAG thin-disk laser," Opt. Lett. **38**, 2422–2424 (2013).
25. P. Rausch, "Deformierbare Spiegel für Weltraumteleskope und Hochleistungslaser," Ph.D. thesis, University of Münster (2016).
26. W. H. Press, S. Teukolsky, W. T. Vetterling, and B. P. Flannery, *Numerical Recipes in C: The Art of Scientific Computing* (Cambridge University, 1992).
27. M. Booth, T. Wilson, H.-B. Sun, T. Ota, and S. Kawata, "Methods for the characterization of deformable membrane mirrors," Appl. Opt. **44**, 5131–5139 (2005).
28. C. Paterson, I. Munro, and J. C. Dainty, "A low cost adaptive optics system using a membrane mirror," Opt. Express **6**, 175–185 (2000).
29. P. Krejci and K. Kuhnen, "Inverse control of systems with hysteresis and creep," IEE Proceedings - Control Theory and Applications **148**, 185–192 (2001).
30. K. Kuhnen, *Inverse Steuerung piezoelektrischer Aktoren mit Hysterese-, Kriech- und Superpositionsoperatoren* (Shaker, 2001).
31. R. A. Muller and A. Buffington, "Real-time correction of atmospherically degraded telescope images through image sharpening," J. Opt. Soc. Am. **64**, 1200–1210 (1974).
32. O. Kazasidis, S. Verpoort, and U. Wittrock, "Algorithm design for image-based wavefront control without wavefront sensing," Proc. SPIE **10695**, 1069502 (2018).
33. D. S. Acton, T. Towell, J. Schwenker, J. Swensen, D. Shields, E. Sabatke, L. Klingemann, A. R. Contos, B. Bauer, K. Hansen, P. D. Atcheson, D. Redding, F. Shi, S. Basinger, B. Dean, and L. Burns, "Demonstration of the James Webb Space Telescope commissioning on the JWST testbed telescope," Proc. SPIE **6265**, 62650R (2006).
34. M. D. Perrin, R. Soummer, É. Choquet, M. N'Diaye, O. Levecq, C.-P. Lajoie, M. Ygouf, L. Lebouleux, S. Egron, R. Anderson, C. Long, E. Elliott, G. Hartig, L. Pueyo, R. van der Marel, and M. Mountain, "James Webb Space Telescope Optical Simulation Testbed I: overview and first results," Proc. SPIE **9143**, 914309 (2014).
35. L. Bliek, H. R. G. W. Verstraete, M. Verhaegen, and S. Wahls, "Online Optimization With Costly and Noisy Measurements Using Random Fourier Expansions," IEEE Transactions on Neural Networks and Learning Systems **29**, 167–182 (2018).
36. H. R. G. W. Verstraete, S. Wahls, J. Kalkman, and M. Verhaegen, "Model-based sensor-less wavefront aberration correction in optical coherence tomography," Opt. Lett. **40**, 5722–5725 (2015).
37. H. R. G. W. Verstraete, M. Heisler, M. J. Ju, D. Wahl, L. Bliek, J. Kalkman, S. Bonora, Y. Jian, M. Verhaegen, and M. V. Sarunic, "Wavefront sensorless adaptive optics OCT with the DONE algorithm for in vivo human retinal imaging [Invited]," Biomed. Opt. Express **8**, 2261–2275 (2017).
38. J. R. Fienup and J. J. Miller, "Aberration correction by maximizing generalized sharpness metrics," J. Opt. Soc. Am. A **20**, 609–620 (2003).

1. Introduction

The Hubble Space Telescope (HST) with a 2.4-m primary mirror had the highest angular resolution in the visible range of all astronomical telescopes for almost 20 years until the early 2010s. The forthcoming James Webb Space Telescope (JWST) has a 6.5-m lightweight, segmented primary mirror, that cannot yield diffraction-limited imaging in the visible. Both HST and JWST have active primary mirrors. The actuators on HST's primary mirror have never been used because its thick mirror turned out to be sufficiently stable, and diffraction-limited resolution was achieved after the COSTAR system was installed [1]. Each of the thin segments of JWST's primary mirror has six actuators for rigid body motions and one actuator for controlling its curvature. JWST will be diffraction-limited in the infrared, but will have an insufficient surface figure for diffraction-limited imaging in the visible.

Space telescopes with angular resolution higher than HST are currently discussed for characterization of exoplanets and for Earth observation from a geostationary orbit. Such telescopes will need to have segmented, lightweight primaries in order to reduce mass and stowed volume. Active optics at the primary mirror and/or in a plane conjugate to the primary mirror will be required. The proposed coronagraph for the WFIRST-AFTA with a 2.4-m primary mirror, which is planned for mid-2020s launch, will use two high-order deformable mirrors to control both the phase and the amplitude of the wavefront, and to keep the phase stable at picometer level [2], which is not required in this work. One of these deformable mirrors will be conjugated to the system pupil and will additionally correct low-order Zernike modes at 5 mHz [3]. The proposed HDST, planned for the 2030s, is envisioned to have a 12-m active segmented primary mirror. The proposed designs for its coronagraph instrument use one or two deformable mirrors [4].

Active and adaptive deformable mirrors often employ actuators which suffer from hysteresis, e.g., piezoelectric actuators. Ground-based astronomical telescopes use natural or artificial guide stars to sense the atmospheric turbulence. Their deformable mirrors are controlled in closed-loop, thereby eliminating the influence of hysteresis. However, it is not possible for every science target to have a sufficiently bright guide star inside the field of view. In addition, direct wavefront sensing using a dedicated wavefront sensor has limited dynamic range and results in non-common path errors.

There exist two main categories of wavefront-sensorless operation, depending on whether the wavefront information is required or not. In the first category, the wavefront information is retrieved by using an indirect iterative method. An example is phase diversity [5–7] that requires two or more measurements of the focal plane intensity taken with different known phase functions physically introduced into the optical system. An estimate for the wavefront is calculated from these measurements and therefore several iterations are required. Finally, the inverse wavefront is applied to the corrective element. In the second category there are completely wavefront-free approaches that do not require the wavefront information, but use the very image captured with the optical system to directly generate the feedback signal for the corrective element. Although here it is not required for the correction, the original aberrated wavefront can be estimated, provided that the corrective element is linear, when the correction is optimal, i.e., the final corrected wavefront is almost plane. The so-called model-based methods model the influence of aberrations in the imaging system. Booth modeled the imaging of a point source in the presence of aberrations with rms amplitudes smaller than 1 rad and expressed as series of Zernike polynomials [8]. He later extended the approach for arbitrarily large aberrations expressed as a series of Lukosz-Zernike functions [9]. Linhai and Rao proposed a general model-based approach insensitive to the selection of the sets of functions [10]. Yang et al. further extended the model to imaging of extended objects [11]. Model-based approaches converge fast at the expense of potential errors due to inaccuracy of the model. On the contrary, model-free approaches need no prior knowledge of the system and iteratively optimize a merit function calculated from the image. These approaches commonly require more iterations, but are simpler, free of modeling errors and uncertainties, and have more general applicability. Model-free wavefront-sensorless adaptive optics has been presented for microscopy [12], optical coherence tomography [13], and ophthalmoscopy [14, 15], among others. The configuration parameters for the control of a model-free wavefront-sensorless adaptive optics system are the merit function, the control domain for the corrective element, and the search algorithm. Their selection and combination depend on the system requirements and are critical for the overall performance.

We designed and built a high-resolution imaging system as testbed for control algorithms for image-based optimization. A space-qualified unimorph deformable mirror based on piezoelectric actuation [16] is at the core of our system. However small the modeling errors of the nonlinearities of the deformable mirror (hysteresis, creep) may be, they become significant for a high-resolution imaging system. Therefore, we implement a model-free iterative control method. Aberrations are

induced by a nominally identical deformable mirror and are corrected in a conjugate plane. Our system resembles that of Murray et al. [17]. They induced Zernike aberrations by a spatial light modulator and corrected them with a membrane deformable mirror using an image sharpness metric and voltage-based global search algorithms. Dong and Yu used a hybrid approach to correct aberrations induced by a trial lens [18]. The correction was carried out in a non-conjugate plane using a membrane deformable mirror. Finally, Agbana et al. experimentally validated the model-based approach of Yang et al. [11], imaging a point source [19]. They induced aberrations with a phase plate and corrected them with a membrane deformable mirror.

In this paper, we investigate guide-star-free, image-based correction of the aberrations of a primary mirror using a unimorph deformable mirror. The deformable mirror is placed in a plane conjugate to the primary mirror and it suffers from hysteresis. We can control the deformable mirror in three different domains, namely the voltage domain, the domain of the Zernike modes, and the domain of its singular modes. We study the merit function near the global optimum and design our control algorithm accordingly. We show the influence of the residual hysteresis of the mirror and demonstrate a combined control scheme that deals with it, accounting for the high dimensionality of the control domains. Finally, we discuss which control domain is more suitable.

2. Experimental method

2.1. Testbed

Our testbed is illustrated in Fig. 1. Static aberrations are deliberately induced by a unimorph deformable mirror (called the *aberration generator*). The aberration correction takes place in a plane conjugate to the aberration generator by a second, nominally identical unimorph deformable mirror (called the *aberration corrector*). The deformable mirrors feature a 50 mm aperture and were developed and manufactured at the Münster University of Applied Sciences. The design, manufacturing and testing of the deformable mirrors are described in [16, 20]. When the aberration generator positioned in plane B is deformed, an aberrated image is formed in plane A′. The aberration corrector is positioned in plane B′, which is conjugated to plane B, and corrects the aberrations. The corrected image is formed in plane A″ and is detected by the CCD.

The object is placed one focal length in front of a converging lens to simulate a distant science target. It is illuminated from the back by a halogen lamp. Homogeneous illumination with a wide spatial frequency content is produced by a ground glass diffuser. Four achromatic doublets from Newport, designed for infinite conjugate ratio, with 76.2 mm diameter are used for relay-imaging. The first three doublets are identical PAC095 with 250 mm effective focal length. The last doublet is a PAC097 with 750 mm effective focal length, leading to a 3x magnification of the object on the CCD. Although the achromats reduce chromatic aberration, they do not eliminate it completely. Therefore, a narrow-band spectral filter with a center wavelength of 632.8 nm and a full width at half maximum of 1.0 nm is placed directly in front of the CCD. The aberration generator is conjugated to the aberration corrector with a unit magnification, which means that at least in principle the aberrations can be fully compensated for an arbitrary wide field of view.

The two deformable mirrors exhibit approximately 40 nm and 17 nm RMS aberration that cannot be compensated for. It consists of print-through and other high-order aberrations. The aperture of the testbed can be adjusted by the iris diaphragm in front of the first achromat. We have stopped down to f/5.4, the maximum diffraction-limited aperture for the achromats. The theoretical cutoff frequency is 290 lp/mm for the wavelength of 633 nm.

We detect the image with a CCD with 4.65 μm pixel size and 5.9 mm × 4.5 mm sensor size, and calibrate it using a master dark frame and a master flat frame. A calibrated image is shown in Fig. 2(a). The limiting resolution of the CCD is 108 lp/mm, which corresponds to 324 lp/mm on the object side. Thus it can detect the theoretical cutoff frequency of the testbed. However, sampling artifacts are expected at spatial frequencies higher than 162 lp/mm in the object [21]. For each experiment we select a region of interest on the CCD, for which we
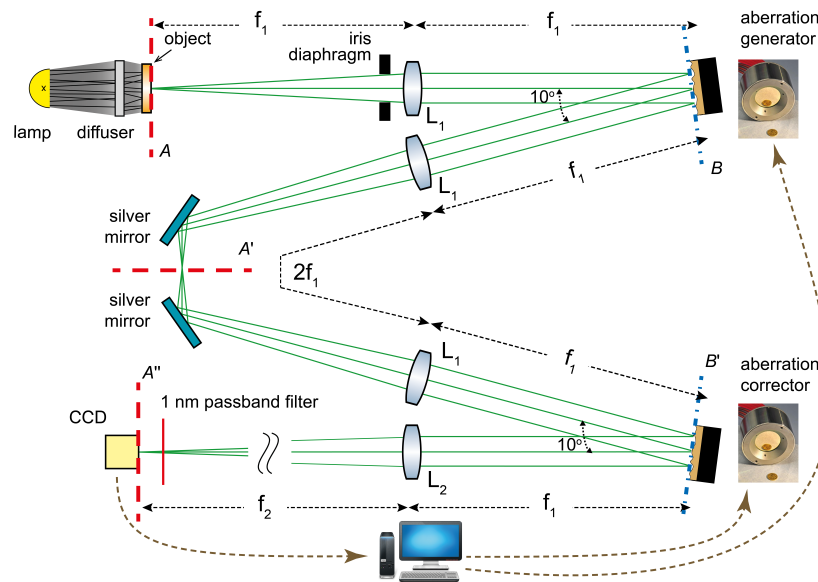
Fig. 1. Sketch of the testbed. The plane of aberration generation (B) is imaged to the plane of aberration correction (B′) with a 4-f telescope and a magnification of −1. The letters A, A′ and A″ indicate the image-forming conjugate planes. The magnification from plane A to plane A′ is −1, and from plane A′ to plane A″ is −3. The angles of incidence on the deformable mirrors are approximately 5°. Due to the non-perpendicular incidence on the deformable mirrors, we place the two silver mirrors around plane A′ to ensure the correct conjugation between the planes B and B′. Lenses focal lengths: $f_1 = 250$ mm, $f_2 = 750$ mm. An image captured with our testbed is shown in Fig. 2.
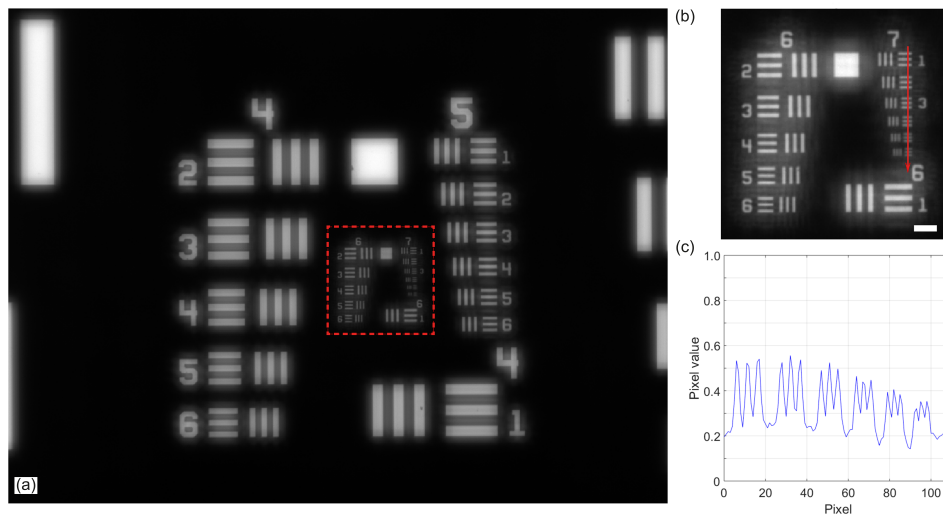

Fig. 2. (a) The detected image with the negative 1951 USAF test target. (b) Highlighted zoom of the image showing the designated region of interest of *a*, with the elements of groups 6 and 7. The white horizontal scale bar in the lower right corner of the image is 31 μm long. (c) The pixel values of the six elements under the red arrow drawn in *b*. The three bars of the sixth element shown at the end of the graph have 228 lp/mm density and are resolved with about 10 % contrast.

calculate the merit function. ZEMAX calculations for the aberration-free scenario showed that diffraction-limited performance is expected for the central $2\,\text{mm} \times 2\,\text{mm}$ of the object, leading to an area of $6\,\text{mm} \times 6\,\text{mm}$ in the image plane, which exceeds the CCD sensor size.

2.2. Deformable mirror control

The surface of the deformable mirrors is controlled by 44 actuators arranged in a keystone pattern. The actuator pattern has been optimized to reproduce low-order Zernike modes up to Z_{12} (secondary astigmatism 45°) with large stroke [22]. Throughout this paper, we use the Zernike notation of Wyant and Creath [23]. The 44 influence functions were captured using a phase-shifting interferometer with 2 nm RMS repeatability and the mirror surface was fitted using 99 Zernike modes [24, 25]. With the same interferometer, we also measured the initial surface deformation of the mirrors and characterized their hysteresis. The influence functions, expressed in 99 Zernike coefficients, are grouped into the columns of the influence matrix ($IM_{99\times44}$). Using the singular-value decomposition (SVD) [26] and applying the Moore–Penrose pseudoinversion we obtain the control matrix ($CM_{44\times99}$):

$$IM = U\ S\ W^T \quad \Rightarrow \quad CM = IM^+ = W\ S^{-1}\ U^T\ , \tag{1}$$

where U, S, and W are the matrices of the SVD. The influence matrix returns the mirror surface in 99 Zernike modes ($\vec{z}_{real}$) when multiplied by a vector containing the voltages that are applied to the actuators of the mirror. In turn, the control matrix gives the required voltages for a desired mirror surface expressed in Zernike modes ($\vec{z}_{des}$):

$$\vec{z}_{real} = IM\ \vec{v} \quad \Rightarrow \quad \vec{v} = CM\ \vec{z}_{des}\ , \tag{2}$$

where $\vec{v}$ is the column vector of the actuators' voltages, and $\vec{z}$ is the column vector of the coefficients of the first 99 Zernike modes that describe the mirror surface. The matrix S of the SVD is diagonal and contains the singular values of the IM in decreasing order. We restrict the condition number (the ratio of the largest singular value to the smallest singular value) of the IM to 200, by truncating the smallest singular values. Thus we keep the pseudoinverse CM well-conditioned. The similarity matrix $IM \cdot CM$ reveals the generation efficiency of the Zernike modes and possible modal cross-talk [27]. The left side of Fig. 3 shows the absolute value of the similarity matrix for the first 41 Zernike modes. The generation efficiency is larger than 0.97 for all Zernike modes up to Z_{12} (secondary astigmatism 45°). For higher-order modes, the generation efficiency is lower and modal cross-talk arises. Z_{15} (secondary spherical aberration) is the first Zernike mode for which the generation efficiency drops below 0.5 (see right plot in Fig. 3). The left side of Fig. 3 shows an example of modal cross-talk: if we want to generate 1 μm of Z_{13} (secondary coma x), we will get a surface with 0.87 μm of Z_{13} and additional higher-order modes, the most prominent of which is Z_{22} (tertiary coma x) with an amplitude of −0.31 μm.

For the correction process we use all the Zernike modes up to the fifth radial order plus some additional higher-order modes up to Z_{32} (quaternary astigmatism 45°). This number is considered to be a good compromise between the generation of sufficiently high spatial frequency deformation that can compensate for hysteresis, and keeping the number of control variables low.

The columns of the matrix W of the SVD make up an orthonormal set and are the *singular modes* of the deformable mirror [28]. The singular modes resemble the mechanical eigenmodes of the mirror. The singular values of the matrix S designate the gain of the corresponding singular mode. The singular modes are related to the actuators' voltages:

$$\vec{s}_{real} = S\ W^T\ \vec{v} \quad \Rightarrow \quad \vec{v} = W\ S^{-1}\ \vec{s}_{des}\ , \tag{3}$$

where $\vec{s}_{real}$ and $\vec{s}_{des}$ are column vectors containing the coefficients of the singular modes. Equation 3 can be used to find the required voltages for a superposition of the singular modes
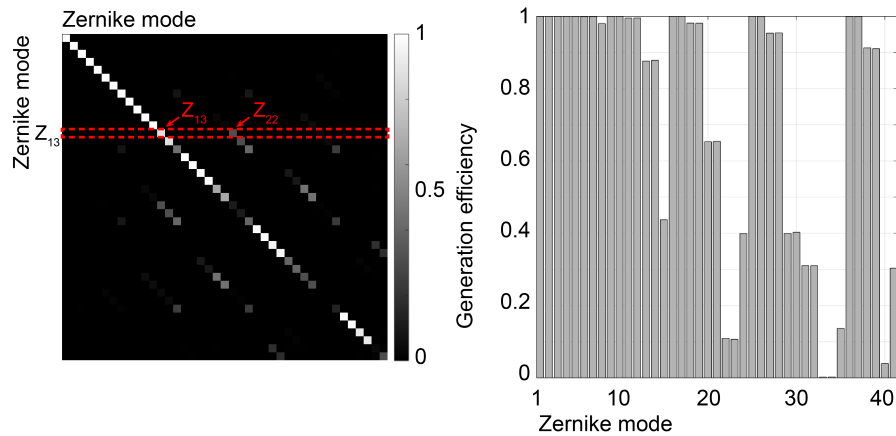
Fig. 3. Left: The absolute value of the similarity matrix for the first 41 Zernike modes for the deformable mirror used as aberration corrector. The matrix is diagonally dominant. The non-zero off-diagonal elements reveal modal cross-talk. An example is marked with red dashed lines: if we want to generate 1 μm of Z_{13}, we will get a surface with 0.87 μm of Z_{13} and −0.31 μm of Z_{22}. Right: The generation efficiency for the first 41 Zernike modes. These are the diagonal elements of the similarity matrix shown on the left.

of the deformable mirror that results in a desired deformation of the mirror. Applying the same restriction for the condition number as above (less than 200), we truncate the 4 singular modes with the smallest gain, leaving 40 singular modes to work with. In contrast to the Zernike modes, the similarity matrix of the singular modes is by definition the identity matrix, leading to a generation efficiency of 1 and no modal cross-talk. In our Zernike representation, the Zernike modes are normalized to the peak-to-valley surface amplitude. For consistency, we also normalized the singular modes to the peak-to-valley surface amplitude. The first 11 singular modes of the aberration corrector are shown in the left plot of Fig. 4. In the right plot of Fig. 4 the normalized singular values of the aberration corrector are drawn, together with the limiting condition number.
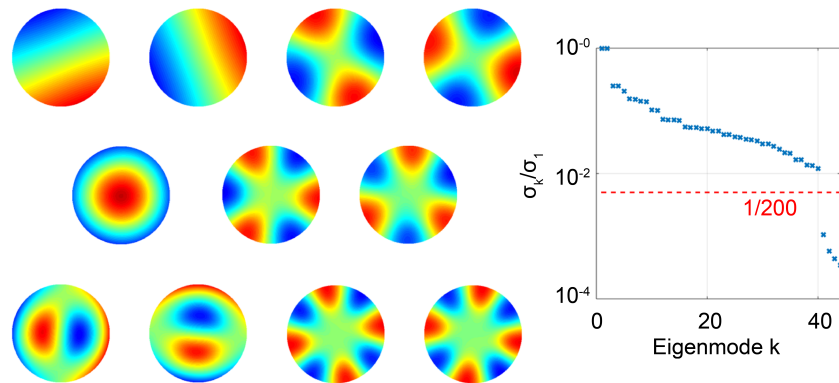

Fig. 4. Left: The first 11 singular modes of the aberration corrector, ordered with decreasing singular value (i.e., gain) from left to right and from top to bottom. They are very similar to low-order Zernike modes. The singular modes are numerically calculated from the experimentally measured influence matrix. Right: The normalized singular values of the aberration corrector. The dashed red line designates the maximum allowed condition number (200), which leads to truncating the 4 smallest singular values.

We control the deformable mirrors in three different domains: 1) by directly selecting the actuators' voltages, 2) by selecting a 99-Zernike-modes vector and calculating the voltages via Eq. (2), and 3) by selecting a 40-singular-modes vector and calculating the voltages via Eq. (3). The piezoelectric hysteresis is compensated open-loop using the Prandtl-Ishlinskii formalism [25], as described in [29, 30]. This reduces the hysteresis from 15 % to 2 %. However, the residual, uncompensated hysteresis of 2 % limits the system performance. The voltages are limited to the range from $-380\,\text{V}$ to $+400\,\text{V}$ in order to protect the actuators. Any voltage vector with values outside this range is rejected using a saturation control.

Figure 5 illustrates the control block diagram of our testbed. An aberration is applied to the aberration generator. The image generated by the testbed and detected by the CCD shown in Fig. 2(a) is evaluated with the merit function. Our algorithm then selects the next vector to be investigated. Depending on the domain, this can be a voltage vector $\vec{v}$, a Zernike vector $\vec{z}$, or a vector of singular modes $\vec{s}$. The output vector is converted to voltages, which are applied to the aberration corrector after passing the open-loop hysteresis compensation and the saturation control.
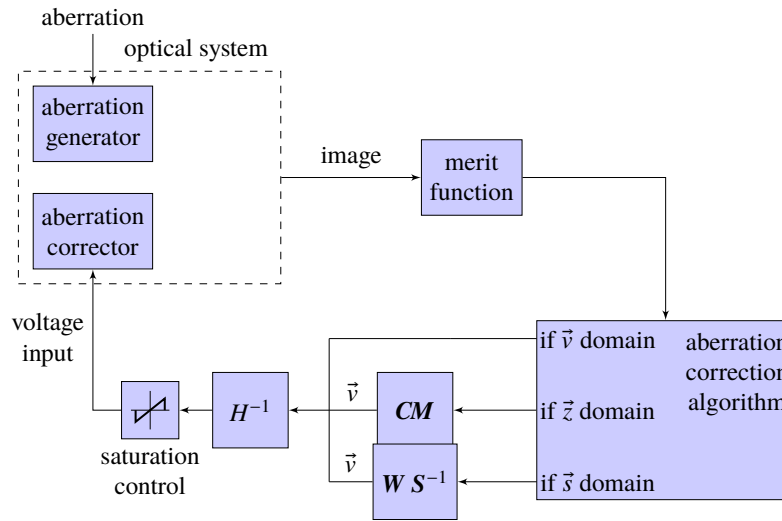

Fig. 5. The control block diagram for the aberration correction. The aberration correction algorithm can be forced to operate in the domain of voltages ($\vec{v}$), Zernike modes ($\vec{z}$), or singular modes ($\vec{s}$). When operating in the Zernike mode domain or in the singular modes domain, the outputs are converted to voltages by matrix multiplication. The control input for the aberration corrector is generated after passing through the open-loop hysteresis compensation (H^{-1}) and the saturation control.

2.3. Merit function

The merit function is calculated only for a certain region of interest, which is a user-defined region of the full image captured with the CCD. Our merit function (MF) is an integral measure of the contrast of the image. We have defined it in the following way:

$$MF = -\frac{\sum_{n_x=1}^{N_x}\sum_{n_y=1}^{N_y} I(n_x,n_y)^2}{\left[\sum_{n_x=1}^{N_x}\sum_{n_y=1}^{N_y} I(n_x,n_y)\right]^2} N_x N_y \ . \tag{4}$$

where x and y are the axes of the image coordinate system within the region of interest, N_x and N_y are the numbers of the pixels in each axis, and I is the pixel output. Our MF is a normalized

discrete version of the common sharpness metric S_1 presented by Muller and Buffington [31]. The normalization has been proposed to account for intensity variations [14]. We have noticed that the non-normalized version can be easier trapped in local minima in case of strong aberrations. The multiplication by the total number of CCD pixels allows the comparison among images of different number of pixels. The minus sign of the MF converts the sharpness maximization to a minimization problem. This merit function is in principle insensitive to image shift. We experimentally determined the random error of our merit function by 300 repetitions of reapplying a specific voltage vector and obtaining the value of the MF when imaging the groups 6 and 7 of the negative 1951 USAF test target. The random error, given by three standard deviations of these 300 values, was $\pm 4.6 \cdot 10^{-3}$ or $\pm 0.3\,\%$, indicating sufficient repeatability.

2.4. Aberration correction algorithm

We set an aberrated surface at the aberration generator. The aberration correction algorithm should then find the surface of the aberration corrector that delivers the minimum merit function, i.e., that maximizes the image sharpness. Our algorithm uses the heuristic hill climbing technique; or rather, in this case of minimization problem, hill descending. It is a model-free black-box optimization, i.e., the algorithm has no analytic form of the MF in relation to the control variables $\vec{v}$, $\vec{z}$, or $\vec{s}$.

The algorithm scans separately each variable, ensuring simple movements inside the search space. We use two routines. The first routine is called *steepest descent in separate variables* and is discussed in detail in [32]. It first calculates the two-sided univariate differentials of the MF. It then runs a hill descending optimization in the direction of the minimum negative differential, i.e. the steepest descent. When this optimization has converged, this variable is removed from the search space and the routine iterates through the rest of the variables. The steepest descent routine ends when all the variables have been optimized, or when all the two-sided univariate differentials are positive, i.e., the MF of the current point is smaller than the MF of every candidate point. The second routine is called *cyclic coordinate descent*. In this routine the MF is also separately minimized with respect to each variable but in a user-defined sequence. The cyclic coordinate descent routine ends when all candidate points of a full cycle have larger MF than the current point.

The first routine needs the two-sided differentials for every variable and chooses the direction of the steepest descent. In the second routine, the user defines the sequence in which the variables are optimized. Therefore, the convergence speed of the second routine strongly depends on the initial point and the variable sequence, and is in general slower than the first routine.

Both routines presented above are deterministic direct local search algorithms. Depending on the MF landscape, the initial point, and the step size, they may get trapped in a local minimum and not return the global minimum. Therefore, in the first experiments of the next section, we study the sensitivity of our MF near the global minimum to detect any other local minima.

3. Results and discussion

We used as object a negative 1951 USAF test target with an optical density ≥ 6 in the visible. An image captured with our testbed is shown in Fig. 2(a). The highest line density of the test target is 228 lp/mm, which should be transmitted by the testbed and is almost equal to its Rayleigh resolution limit (238 lp/mm). We preferred the 1951 USAF pattern over the NBS 1963A pattern because it uses space more efficiently, allowing many spatial frequencies to be in the image simultaneously. The region of interest for the calculation of the merit function is the central part of the image, including the elements of groups 6 and 7 (as in Fig. 2(b)).

3.1. Merit function sensitivity

We first studied the sensitivity of the merit function with respect to variations of the variables of the three different control domains (voltage domain, Zernike mode domain, and singular modes domain) of the aberration corrector near the global minimum. For these experiments the aberration generator was open-loop flattened by applying the opposite of its initial surface deformation, which was measured by the phase-shifting interferometer as described in section 2.2. The global minimum for the aberration corrector was found with a cyclic coordinate descent in the voltage domain, the Zernike mode domain, or the singular modes domain. There is no simple relation between the optical resolution and the merit function of Eq. (4). We characterized the region of the global minimum of the MF by visually ensuring that the highest line density of the test target which is near the diffraction-limited resolution limit was resolved. From that initial state, in each experiment one variable was changed stepwise in a predefined range, first increasing to the upper bound, then decreasing to the lower bound, and finally increasing to its initial value. In each step the MF was calculated. Thus in the resulting 1D-cuts of the MF we can detect possible local minima that may trap a local search algorithm.

We varied the voltages of all 44 actuators by ±20 V from their values at the global minimum of the merit function. This range corresponds to $1/20$ of the operational voltage range. The actuators are physically arranged in rings [22]. As can be seen in the inset of Fig. 6, the actuator 1 is the inner actuator, the actuators 2 to 9 form the first ring, the actuators 10 to 25 form the second ring, and the actuators 26 to 41 form the third ring, which is outside of the clear aperture of the deformable mirror. Finally, the actuators 42 to 44 are at the outer mounting ring and serve for tip/tilt generation. The voltages of the actuators of the same ring exhibit similar sensitivity. Therefore, only the sensitivity plot for one actuator per ring and all actuators of the outer mounting ring are shown in Fig. 6. The MF has a single minimum for V_1 to V_{41}. The sensitivity decreases as we move to the outer rings. Later we discuss the plots for V_{42} to V_{44}.
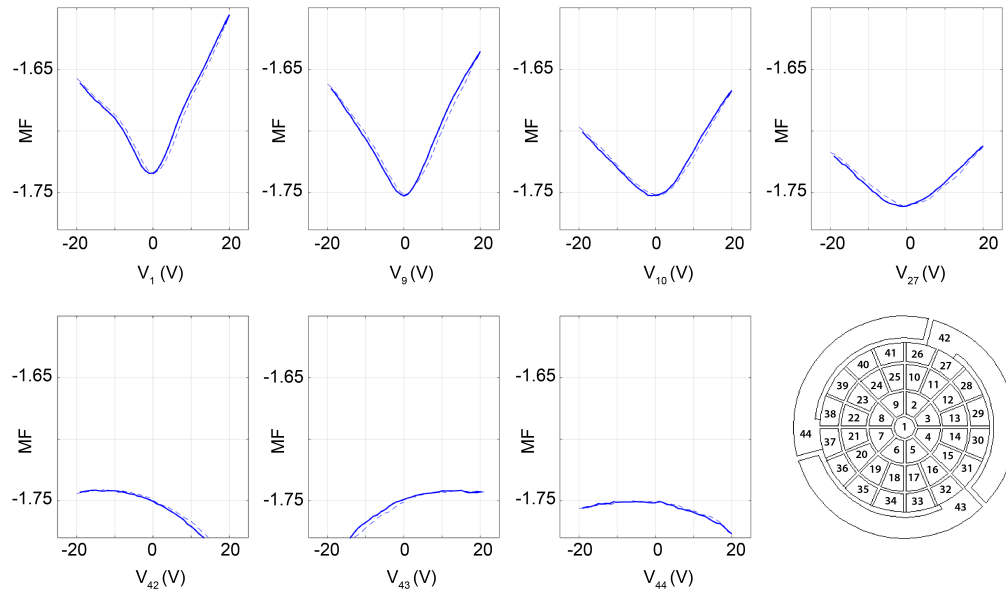

Fig. 6. The merit function in the voltage domain for the actuators 1, 9, 10, 27, 42, 43, and 44. The plots are centered to the voltage values at the global minimum of the merit function. The solid line corresponds to decreasing amplitude and the dashed line to increasing amplitude. The small difference between the two lines is caused by residual uncompensated hysteresis. The inset at the lower right corner shows the actuator pattern and numbering.
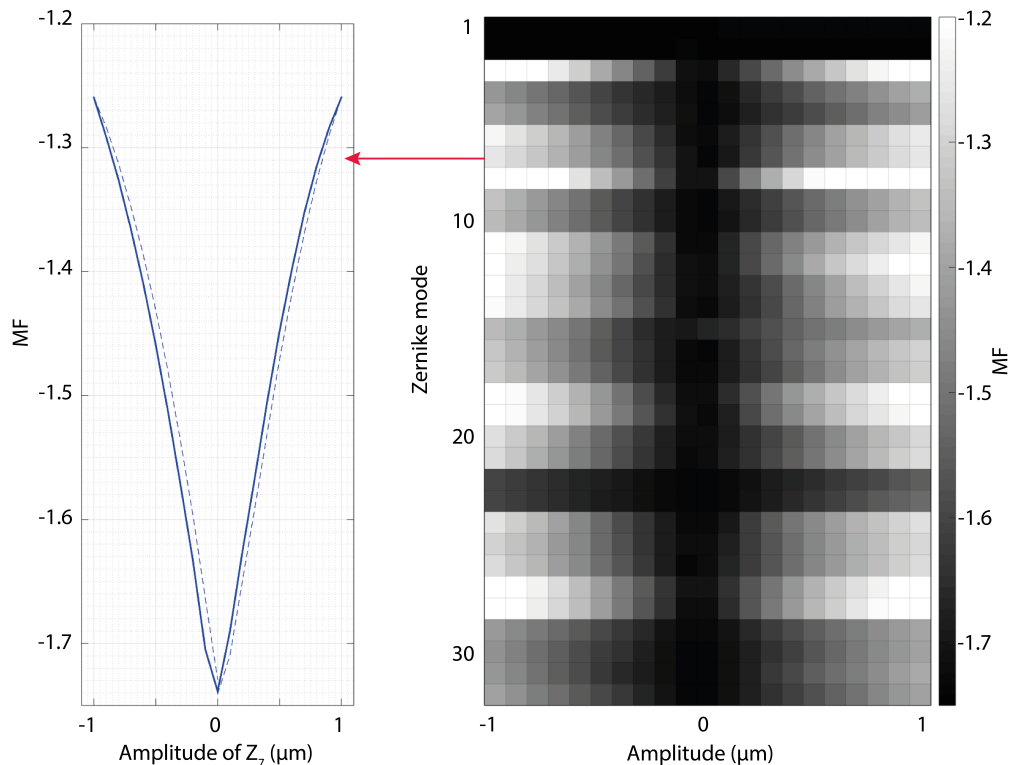
Fig. 7. The merit function in the Zernike mode domain. Left: The full sensitivity plot for Z_7 (coma y). The solid line corresponds to decreasing amplitude and the dashed line to increasing amplitude. The small difference between the two lines is caused by residual uncompensated hysteresis. Right: The MF for decreasing amplitude from 1 μm to −1 μm in grayscale. Each row of the matrix corresponds to one Zernike mode from Z_1 to Z_{32}.

In the Zernike mode domain, we varied the amplitude of the Zernike modes up to Z_{32} (quaternary astigmatism 45°) in the range of ±1 μm from their values at the global minimum of the merit function. The full sensitivity plot for Z_7 (coma y) is shown in the left side of Fig. 7. The MF for decreasing amplitude for each Zernike mode is shown in grayscale in the right side of the figure. The low sensitivity of the MF to image shift is apparent in the rows for Z_1 (tip x) and Z_2 (tilt y).

In the singular mode domain we varied the amplitude of the first 32 singular modes in the range of ±1 μm from their values at the global minimum of the merit function. The full sensitivity plot for E_8 is shown in the left side of Fig. 8. The MF for decreasing amplitude for each singular mode is shown in grayscale in the right side of the figure. The low sensitivity of the MF to image shift is again apparent in the rows for E_1 and E_2, the first two singular modes which are combinations of tip and tilt, as shown in Fig. 4.

We first discuss the influence of image shift. The MF was calculated for the region of interest, defined as a specific part of the CCD. Our MF is insensitive to an image shift on a constant background, but it decreases when the shift moves the image outside the region of interest. The background of our image is not constant and varies spatially, because the nominally black pixels have actually different non-zero values due to limited contrast of the test target, diffraction, and residual aberrations. The MF depends also on the phasing between the image and the CCD pixels,
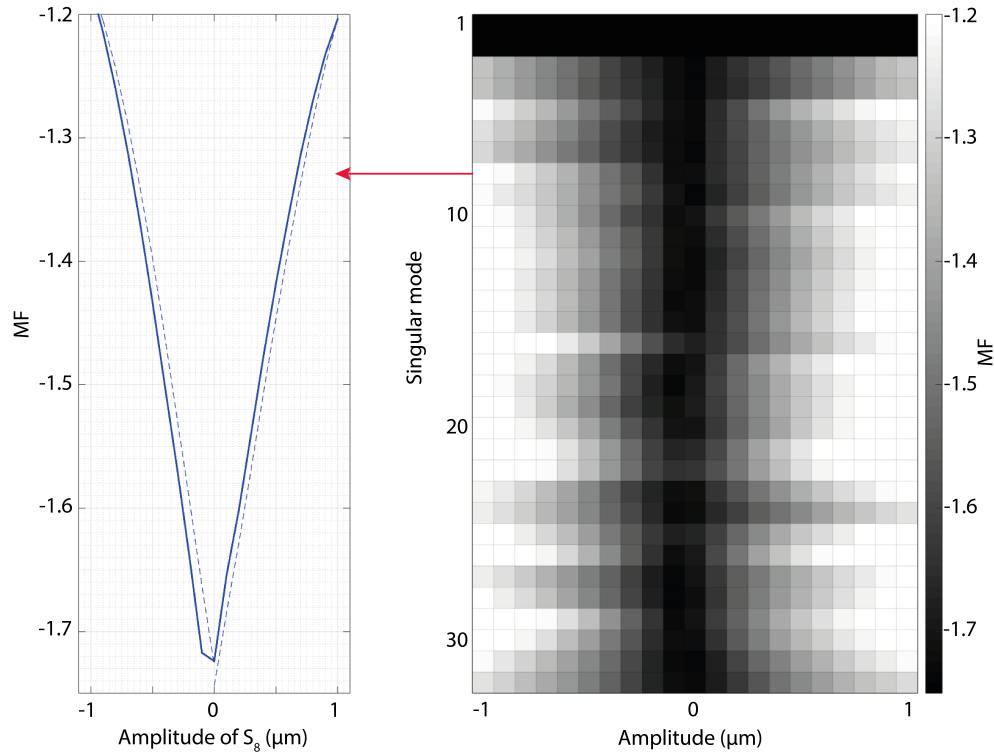
Fig. 8. The merit function in the singular mode domain. Left: The full sensitivity plot for S_8. The solid line corresponds to decreasing amplitude and the dashed line to increasing amplitude. The small difference between the two lines is caused by residual uncompensated hysteresis. Right: The MF for decreasing amplitude from 1 μm to -1 μm in grayscale. Each row of the matrix corresponds to one singular mode from S_1 to S_{32}. The first 11 singular modes are shown in Fig. 4.

which changes with shift. The above explain the non-constant sensitivity plots of the MF for V_{42} to V_{44} in Fig. 6. The sensitivity plots of the MF for the Zernike modes Z_1 and Z_2, and the singular modes S_1 and S_2 that lead to image shift are also non-constant, which is not apparent in Figs. 7 and 8 due to the scaling. Image registration would eliminate the dependence from image shift. However, we do not currently apply it, because of its increased complexity. To minimize the effects of image shift we decouple the correction process from it, excluding the Zernike modes Z_1 and Z_2, and the singular modes S_1 and S_2 from our algorithm. In the voltage domain, the influence matrix shows that every actuator, except actuator 1, produces image shift. The reason is that all actuators except this one are located off-axis and therefore produce overall tip or tilt. We exclude the voltages $V_{42} - V_{44}$ which contribute almost exclusively to image shift. This procedure conforms with the common practice of image stabilization using a separate tip/tilt mirror, e.g., the fine steering mirror in JWST.

Figures 6 to 8 show that near the global minimum the 1D-cuts of the merit function exhibit no other local minima and no plateaus. Therefore, our routines presented in section 2.4 are appropriate for the minimization of the MF in all three control domains. In [32] we further studied the merit function landscape, by examining 2D-cuts both numerically and experimentally.

We emphasize the open-loop control of the deformable mirror, as described in section 2.2. The shown voltage values, Zernike mode coefficients, and singular mode coefficients were the

inputs of the control system and did not necessarily correspond to the actual mirror state. For the Zernike mode domain in particular, the use of the pseudoinverse $\boldsymbol{CM}$ after truncating the smallest singular values generates a voltage vector $\vec{v}$ that corresponds to the least-squares solution for the mirror surface. Therefore, the generated mirror surface in Zernike modes $\vec{z}_{real} = \boldsymbol{IM}\,\vec{v}$ differs from the desired mirror surface $\vec{z}_{des}$, and the voltage vector minimizes the residual error $\left|\boldsymbol{IM}\,\vec{v} - \vec{z}_{des}\right|$ [26]. For example, the generation efficiency of the Zernike modes Z_{22} and Z_{23} (tertiary coma x and y, respectively) is just 0.1 (see Fig. 3); this leads to the low sensitivity of the MF shown in the corresponding plots in Fig. 7.

3.2.   *Hysteresis compensation*

The sensitivity plots of the merit function of Figs. 6 to 8 are at the same time the hysteresis loops of the MF, revealing any residual hysteresis after the open-loop compensation using the Prandtl-Ishlinskii (PI) formalism we mentioned in section 2.2. We quantify the hysteresis by using the 1-D cuts of the merit function near the global minimum. We can use two quantities calculated between the decreasing and the increasing part of the loop: the horizontal shift of the minimum of the MF, and the maximum horizontal opening of the butterfly-like loop. Both quantities are given as ratio with respect to the width of the control variable's range. The loops are rather narrow (maximum horizontal opening of about 2.5 %) in the voltage domain, and become slightly wider and more complex for some modes in the Zernike mode domain and in the singular mode domain, because of the concurrent actuation of more than one actuator.

Here we examine the reaction of our algorithm to hysteresis more closely. The left side of Fig. 9 shows the sensitivity plots of the MF for the Zernike mode Z_9 (trefoil 0°) with and without the open-loop hysteresis compensation in the range (−2 μm, +2.1 μm) from its value at the global minimum of the merit function. The horizontal shift of the minimum of the MF is 4.9 % with the open-loop PI hysteresis compensation, and 17 % without the open-loop PI hysteresis compensation. The horizontal shift means that we can counteract the hysteresis by readjusting just the amplitude of the Zernike mode Z_9. The minimum of the MF also shifts vertically. The vertical shift, which is larger without the open-loop PI hysteresis compensation, means that this hysteresis cannot be compensated solely with Z_9. The Zernike modes are orthogonal and the singular modes are orthogonal as well. However, in the presence of hysteresis the voltage patterns that correspond to different Zernike modes are no longer orthogonal and the same holds true for the voltage patterns that correspond to different singular modes. This is obvious because the voltage pattern that creates a certain Zernike mode or singular mode is not unique but depends on the previous state of the mirror. The width of the hysteresis loop and the shift of the minimum of the MF varies among the Zernike modes and depends on the number and the position of the actuated actuators, and on the voltage values. The loop without hysteresis compensation for Z_9 shown in the left side of Fig. 9 is the most extreme of all low-order Zernike modes. For Z_4 (astigmatism 0°) we only observed a horizontal shift of the loop. For Z_3 (defocus) and Z_6 (coma x) a relatively small vertical shift was observed.

From the above analysis we deduce that the actuation of a Zernike mode may induce hysteresis that requires other Zernike modes for compensation. Therefore we cannot significantly reduce the dimensionality of the Zernike mode domain (nor of the singular mode domain) for the aberration correction algorithm. The right side of Fig. 9 shows another experiment that further demonstrates the influence of the residual hysteresis on our testbed, which remains after the open-loop PI hysteresis compensation. With the aberration generator open-loop flattened, we found the global minimum of the MF for the aberration corrector with a cyclic coordinate descent in the Zernike mode domain. We then successively set 100 random voltage patterns at the aberration corrector. Such random voltage vectors are used by global search evolutionary algorithms. Finally, we set again the voltages corresponding to the values at the previously found global minimum of the MF. Due to the residual hysteresis, the merit function deviates by approximately 12 % from its
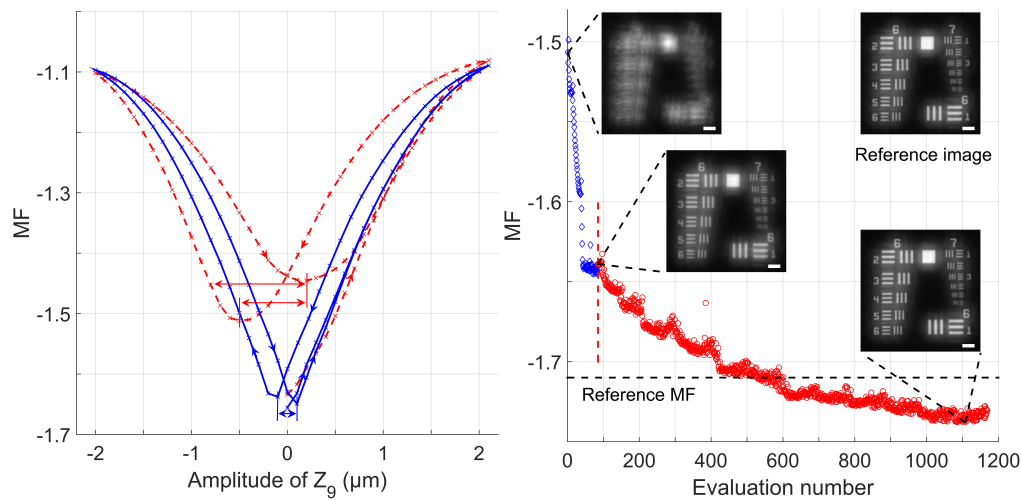
Fig. 9. Left: Sensitivity plots of the MF for Z_9 (trefoil 0°) with (blue solid line) and without (red dashed line) the open-loop hysteresis compensation. The curves start at $Z_9 = 0\,\mu m$, and $MF = -1.66$ (blue) and $MF = -1.63$ (red). The horizontal shift of the minimum of the MF is 0.2/4.1=4.9 % (blue double-headed arrow) and 0.7/4.1=17 % (lower red double-headed arrow), respectively. When the open-loop hysteresis compensation is active, the maximum horizontal opening is equal to the horizontal shift of the minimum, i.e., 4.9 % (blue double-headed arrow). When the open-loop hysteresis compensation is inactive, the maximum horizontal opening is 1.0/4.1=24 % (upper red double-headed arrow). Right: Compensation of the residual hysteresis with an algorithm in Z_3 to Z_5 (blue diamonds) followed by an algorithm in voltages (red circles). The white horizontal scale bar in the lower right corner of the images is 31 μm long.

original minimum. We compensated this deviation by using a cyclic coordinate descent in the Zernike modes Z_3 to Z_5 (defocus and the two primary astigmatisms), followed by another cyclic coordinate descent in voltages. The algorithm in the three low-order Zernike modes Z_3 to Z_5 improved the merit function fast and efficiently by 9 %, leaving a 4 % deviation from the original minimum. The algorithm in the voltage domain was significantly slower because the voltage search space has a larger dimension than the Zernike mode search space, but converged to a merit function even lower (better) than the original minimum. This is attributed mainly to high spatial frequency deformation that could not be corrected in the Zernike mode domain in the first search for the minimum. Another, though lesser, influence had the image shift that was discussed in detail in the previous section.

3.3. Correction of Zernike aberrations

In the next experiments, we show the correction of single Zernike aberrations. Before each experiment, the aberration generator was open-loop flattened and we found the global minimum of the merit function for the aberration corrector, as described in section 3.1. An image was taken at this state of the two deformable mirrors and we call this the "reference image". Then, we applied to the aberration generator a single Zernike aberration from the range Z_3 (defocus) to Z_{10} (trefoil 30°) with 1 μm amplitude. Finally, we ran a steepest descent in the Zernike modes Z_3 to Z_{10}, followed by a cyclic coordinate descent in the Zernike modes Z_3 to Z_{32}. The steepest descent corrects the largest part of the aberrations. The cyclic coordinate descent performs the fine-tuning and compensates for residual hysteresis and high-order deformations that cannot be represented by the low-order Zernike modes Z_3 to Z_{10}. The results are summarized in Fig. 10.

The open-loop, nominally pure single-Zernike aberration produced by the aberration generator was predominantly corrected by the aberration corrector by the same Zernike mode with opposite sign. This mode made up at least 95 % of the squared amplitudes of the superposition of Zernike modes that the algorithm produced. The non-zero values of other Zernike modes are attributed to residual hysteresis and errors in the alignment and optical conjugation between the two deformable mirrors. The MF of the corrected images was up to 55 % lower than that of the aberrated images and in very good agreement with the MF of the reference images (2.1 % maximum deviation). Only when Z_8 (spherical aberration) had to be corrected there was a 10 % residual deviation from the reference image and the test target was not fully resolved. However, there was a 51 % improvement from the aberrated image. The generation of Z_8 is expensive in terms of voltage and actuator dynamic range. This led to significant uncompensated hysteresis which included high-order deformation that could not be fully corrected in the Zernike mode domain. We could further improve the MF by using a cyclic coordinate descent in voltages (not shown).
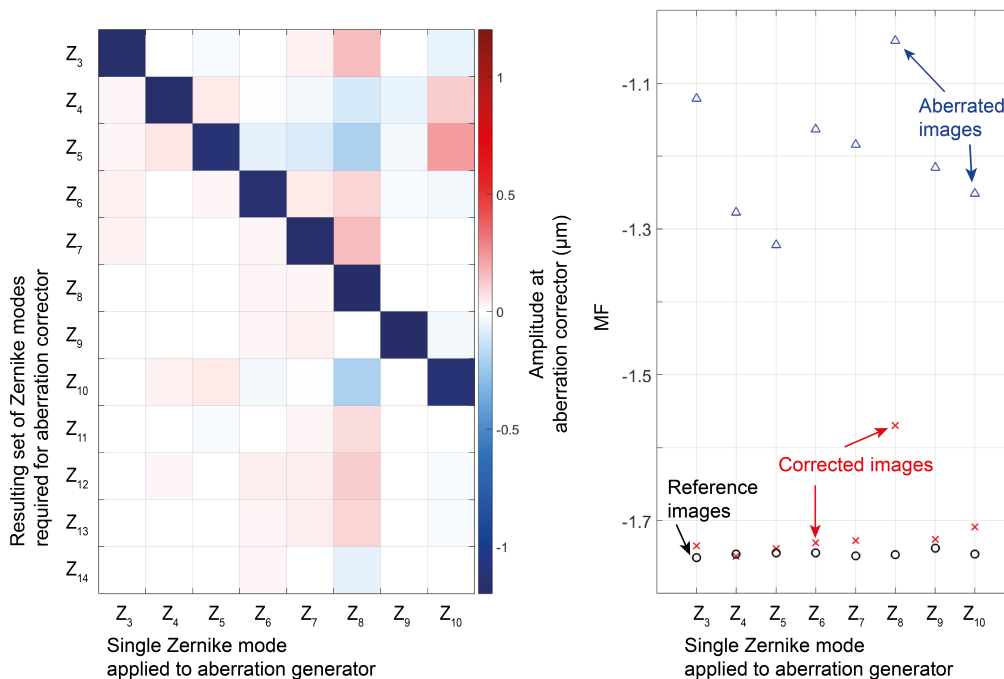

Fig. 10. The results of the single Zernike aberration experiments of 1 μm amplitude. Left: The output of the correction process in Zernike modes in color code. Each column of the matrix refers to an experiment when a single Zernike aberration was applied to the aberration corrector. Ideally the matrix would be diagonal with all the diagonal elements equal to −1. To save space we do not show the modes Z_{15} to Z_{32}, whose maximum absolute value is 0.1 μm. Right: The merit function of the reference images (black circles), the aberrated images (blue diamonds), and the corrected images (red crosses).

In the next experiment, we set a superposition of Zernike modes at the aberration generator. For the correction we applied two consecutive steepest descents in the Zernike modes Z_3 to Z_{10}, followed by a cyclic coordinate descent in the Zernike modes Z_3 to Z_{32}. In the example shown in Fig. 11, we set the aberration vector $\vec{z}_{ab} = -0.8\,\mu m\ Z_4 + 1.0\,\mu m\ Z_6 + 0.6\,\mu m\ Z_9 - 0.5\,\mu m\ Z_{10}$, i.e., astigmatism 0°, coma x, trefoil 0°, and trefoil 30° with the corresponding amplitudes. The two runs of steepest descent corrected the largest part of the aberrations, improving the MF by 35 %. The cyclic coordinate descent fine-tuned the image, further improving the MF by 5.8 %.
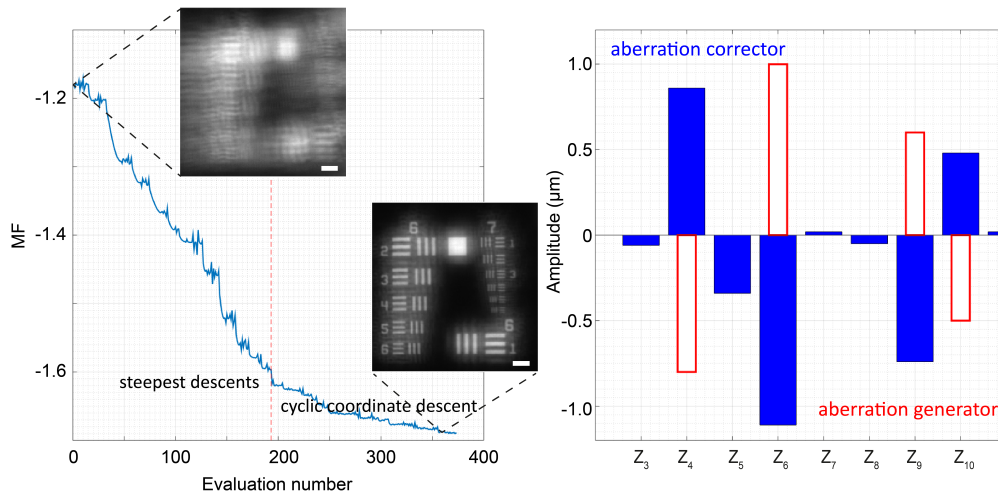
Fig. 11. Left: Progress of the correction for a combination of Zernike modes. The steepest descents correct fast most of the aberrations and the cyclic coordinate descent fine-tunes the image. The aberrated image and the corrected image are shown. The white horizontal scale bar in the lower right corner of the images is 31 µm long. Right: The coefficient of the Zernike modes for the aberration generator (red unfilled bars) and for the aberration corrector (blue filled bars).

The amplitudes of the Zernike modes of the aberration corrector were almost equal to those of the aberration generator with opposite sign, as shown in the right plot of Fig. 11. The only major exception is Z_5 (astigmatism 45°), whose non-zero value is attributed to hysteresis and system misalignments. The corrected MF was 43 % lower (better) than the aberrated MF, and it deviated by 2.6 % from that of the reference image (not shown).

3.4. Correction of aberrations produced by random voltages

Here we compare the correction in the Zernike mode domain and in the singular mode domain. As in section 3.3, the aberration generator was open-loop flattened before each experiment, the algorithm found the optimum surface for the aberration corrector and a reference image was taken. Then, we added a random voltage vector at the aberration generator to create a superposition of the influence functions. Thus the initial point of our algorithm was away from the global minimum and we could study the influence of the complexity of the MF landscape on our algorithm. The left plot of Fig. 12 shows the voltage values obtained from the uniform random distribution in the interval (-25 V, $+25$ V). To prevent image shift we used the influence matrix and set the Z_1 (tip x) and Z_2 (tilt y) to zero. In the right plot of Fig. 12 we compare the performance of the aberration correction in the Zernike mode domain and in the singular mode domain. In each domain we ran a cyclic coordinate descent for the modes from 3 to 32. The optimum MF obtained in the Zernike mode domain was 16 % lower (better) than that of the aberrated image and deviated by 7.7 % from that of the reference image (not shown). The optimum MF obtained in the singular mode domain was 24 % lower (better) than that of the aberrated image and deviated by just 1.1 % from that of the reference image (not shown).

Both the used Zernike mode domain and singular mode domain have the advantage of reduced dimensionality in comparison to the voltage domain. In the singular mode domain, the selection of the variables and the dimensionality reduction are straightforward. The singular modes contribute to the mirror surface with a gain given by their singular values. Thus we can select the appropriate
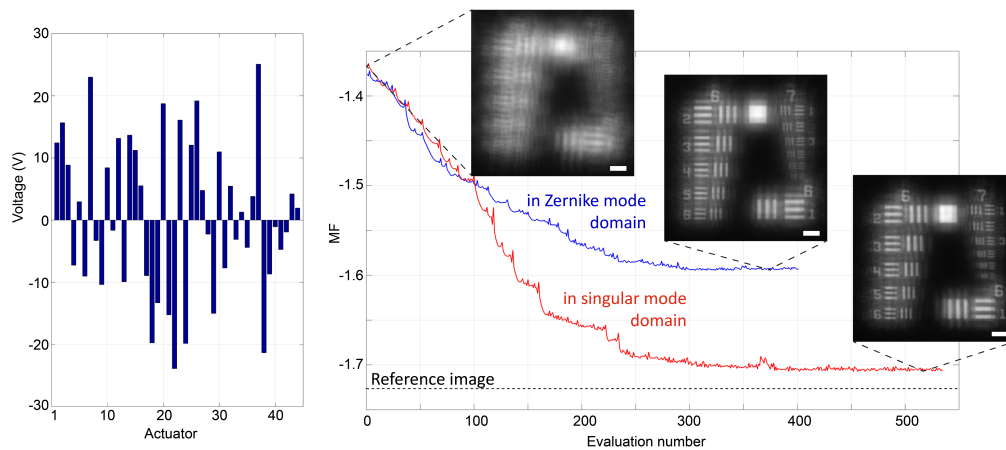
Fig. 12. Left: The voltages set at the aberration generator, randomly chosen in the interval (−25 V, +25 V). Right: Comparison of the aberration correction in the Zernike mode domain and in the singular modes domain. The correction in the Zernike mode domain requires less evaluations for convergence of the MF, but results in a poorer MF than the correction in the singular mode domain. The white horizontal scale bar in the lower right corner of the images is 31 μm long.

singular modes for the correction by inspecting the singular values (see Fig. 4) and add modes until we reach the desired accuracy. In the Zernike mode domain, the selection of the variables is not trivial. In this example, we chose all modes up to the Zernike mode Z_{32}. Apparently this was not enough in order to represent the superposition of the influence functions generated by the random voltages of the aberration generator. We can increase the dimensionality of the Zernike mode domain by adding more Zernike modes, at the expense of slower convergence. By intuition we can select only the Zernike modes with high generation efficiency (see Fig. 3). However, we thus may still not be able to generate the aberration created by a random voltage vector. There exists no clear indication how many and which Zernike modes we should include in the correction of random aberrations.

On the other hand, there is always the possibility that the algorithm in the Zernike mode domain got trapped in a local minimum. A random voltage vector leads to complex aberrations in the Zernike mode domain and we cannot predict the MF landscape by inspecting the simple 1D-cuts near the global minimum (shown in Figs. 6 to 8) or even the 2D-cuts (shown in [32]).

4. Summary and conclusions

With a view to the next generation of large space telescopes, we designed and built a high-resolution imaging system as testbed for image-based aberration correction. Image-based aberration correction could be an alternative or a complement to wavefront sensing via phase diversity as used by JWST and demonstrated on its testbeds [33, 34].

We reported the results of our systematic experimental study for control in three different domains, namely the voltage domain, the domain of the Zernike modes, and the domain of the singular modes of our deformable mirror. Table 1 summarizes the identified advantages of each control domain. The image-sharpness metric applied as merit function has no other local optima near the global optimum, allowing the use of a local search algorithm. We demonstrated a combined control scheme that deals with the residual hysteresis left over by a Prandtl-Ishlinskii compensation and with the high dimensionality of the control domains. Our algorithm corrected aberrations produced by random voltages better when operating in the singular mode domain

than in the Zernike mode domain. We used two nominally identical deformable mirrors for aberration generation and aberration correction. This is an idealized, yet in many ways realistic, scenario. The deformable mirror conjugated to the entrance pupil of a large space telescope should be physically designed to compensate for the expected deformation of the primary mirror by matching its singular modes to those of the primary mirror. The required demagnification would in this case restrict the aberration correction to a limited field of view.

Table 1. The advantages of each domain for the wavefront-sensorless control of a deformable mirror (DM) with hysteresis in an imaging system.

	Advantages
Voltage domain	- spans the full capability of the DM
	- directly connected to the hysteresis
Zernike mode domain	- associated with the optical performance
	- possible, but nontrivial, reduction of search space
Singular mode domain	- connected to the mechanical properties of the DM
	- possible straightforward reduction of search space

We are currently testing the Data-based Online Nonlinear Extremum-seeker (DONE) algorithm [35] in our testbed for the case of small aberrations. The DONE algorithm was demonstrated for wavefront-sensorless adaptive optics in optical coherence tomography [36] and has already been used with a multi-actuator adaptive lens that suffers from hysteresis [37]. Our control can be further extended by using a model-based approach, e.g., as proposed by Yang et al. [11]. Due to the nonlinearities caused by the hysteresis of our deformable mirror, a model-free approach will still be required at the final stage. However, the convergence speed is expected to increase significantly. In addition, other merit functions can be tested, such as the generalized sharpness metrics proposed by Fienup and Miller, which exploit the characteristics of the object [38]. This can become particularly significant in the case of Earth observation, where the sharpness metric can be optimally designed depending on the image type of the application (e.g., urban areas, forests, maritime surveillance). In the current state of our testbed, the deformable mirrors require an external calibration stage for the measurement of their influence functions and the characterization of their hysteresis. A more elaborate wavefront-sensorless approach would be able to calibrate the deformable mirror directly in the testbed, or in the space telescope after deployment, e.g., by using phase diversity and imaging a well-known target, and thus would not require any direct wavefront measurement.